Flexible PAN-$Bi_2O_2CO_3$-BiOI heterojunction nanofiber and the photocatalytic degradation property

Pingping Teng[a], Jiabao Zhu[a], Zhiang Li[a], Kang Li[b], NigelCopner[b], Shuai Gao[a,*], Enming Zhao[c], Xiaoliang Zhu[d], Zhihai Liu[a,*], Fengjun Tian[a], Yu Zhang[a]

[a]Key Laboratory of In-Fiber Integrated Optics, Ministry of Education, College of Science, Harbin Engineering University, Harbin 150001, China

[b]Wireless & Optoelectronics Research & Innovation Centre, Faculty of Computing, Engineering & Science, University of South Wales, Wales, CF37 1DL, UK

[c]School of Engineering, Dali University, Dali 671000, China

[d]Zhejiang Gongshang University, School of Information&Electronic Engineering (Sussex AI Institute), Hangzhou 310018, China

[*] Corresponding author

shuai.gao@hrbeu.edu.cn; liuzhihai@hrbeu.edu.cn

Abstract

In this paper, one-dimensional PAN-$Bi_2O_2CO_3$-BiOI photocatalytic nanofibers were prepared using flexible PAN nanofibers as carriers. $Bi_2O_2CO_3$ was first grown on the surface of PAN nanofibers, and then BiOI was loaded on $Bi_2O_2CO_3$ by ion exchange method. The characterization results showed that PAN-$Bi_2O_2CO_3$-BiOI nanofibers have a diameter of about 210 nm and regular fiber morphology. The results of UV-Vis diffuse reflectance spectroscopy, XRD and XPS showed that $Bi_2O_2CO_3$-BiOI composed of granular semiconductor nano heterostructures with high specific surface area were uniformly loaded on the surface of PAN fiber. The photocatalytic degradation experiment of the material showed high visible light photocatalytic activity. The preparation of $Bi_2O_2CO_3$-BiOI heterojunction improved the photoelectron hole separation efficiency of BiOI under visible light. PAN-$Bi_2O_2CO_3$-BiOI fibers showed high photocatalytic degradation efficiency for rhodamine B. The degradation efficiency was more than 95% within 120 min irradiation. Free radical trapping experiments showed photocatalysts mainly produced O_2^-,·OH and h^+, which played a major role in photocatalysis.

Keywords: $Bi_2O_2CO_3$-BiOI heterojunction; electrospinning; photocatalytic; degradation

1. Introduction

In recent years, the problem of environmental pollution caused by organic pollutant has become increasingly serious, and photocatalyst technology has gradually become an effective means to control organic pollution [1-7]. The main factor influence the application of photocatalytic technology is low efficient utilization of visible light. At present, doping, photosensitization and semiconductor are the main methods to expand the wavelength range of photocatalytic utilization to visible light and improve their photocatalytic activity. Especially, semiconductor photocatalytic materials have the characteristics of high specific surface area and tunable band gap by constructing heterojunctions, which can significantly improve the electron-hole separation efficiency under the irradiation of visible light thereby improving the photocatalytic activity [8-15]. Simultaneously, visible light photocatalytic oxidation technology has mild reaction conditions. By adjusting the band gap width, semiconductor photocatalytic materials can degrade macromolecular organic pollutants into non-toxic small molecular compounds under sunlight illumination conditions.

Among them, bismuth semiconductors (bismuth tungstate, bismuth vanadate, bismuth halide, bismuth titanate, bismuth oxycarbonate, etc.) have attracted increasing attention because of their high carrier concentration due to the layer nanocrystal structures and the internal electrostatic field [16-22]. Especially, $Bi_2O_2CO_3$ photocatalyst, as a new type of semiconductor photocatalytic material, has layered structure and suitable forbidden band width (about 3.20 eV) [23-25]. It is an Aurivillius-type oxide composed of alternating layers of $[Bi_2O_2]^{2+}$ and CO_3^{2-}. $Bi_2O_2CO_3$ shows great potentials in photocatalytic oxidation and degradation of organic pollutants [26, 27]. However, the nanometer $Bi_2O_2CO_3$ catalyst has the problems of difficulty in separation and secondary pollution [28]. At the same time, pure phase $Bi_2O_2CO_3$ has a higher electron-hole carrier recombination probability which limits its catalytic performance.

In addition, bismuth oxyhalide (such as BiOCl, BiOBr, and BiOI) is a class of indirect band gap semiconductor which has wide band gap and strong photochemical stability [29-31]. In BiOX (X=Cl, Br, I), the photoelectrons usually pass through the k-space and back to the valence band. It will reduce the carrier current. This process will promote the separation of photogenerated electron hole in it. In particular, bismuth halide (BiOI) with layered atomic arrangement and unique electronic structure has a narrow band about 1.8 eV and strong absorption in the visible

light region [32-35]. Considering that both BiOI and $Bi_2O_2CO_3$ contain bismuth ion, $Bi_2O_2CO_3$-BiOI heterojunction can be constructed by ion exchange method by generating BiOI on the surface of $Bi_2O_2CO_3$ [36,37]. On the other hand, electrospun fibers with high specific surface area are widely concerned in visible-light photocatalysis [38-40]. Compared with the direct doping method, the growth of catalyst on the surface of electrospun fiber is easy to increase load capacity. Especially, PAN electrospun nanofiber with smooth surface is more suitable as a catalyst carrier because it is stable in water phase. Moreover, the flexible disordered fibers constitute a macroscopic mesh structure and is convenient for separation, recovery and reuse of the catalyst. Therefore, electrospun PAN nanofibers are suitable as the carrier to solve the difficulty of agglomeration and recycle of catalyst.

In this paper, we use electrospun PAN as a template to grow $Bi_2O_2CO_3$ nanoparticles on its surface by the alternate growth method, and then to grow BiOI on the $Bi_2O_2CO_3$ surface by the ion exchange method to form $Bi_2O_2CO_3$-BiOI photocatalytic heterojunctions.

2. Experimental section

2.1. Chemicals

All the reagents in this study are of analytic grade and used without further purification. Bismuth nitrate pentahydrate ($Bi(NO_3)_3 \cdot 5H_2O$) was purchased from Shanghai Macklin biochemical technology Co., Ltd. Potassium iodide (KI) and anhydrous sodium carbonate (Na_2CO_3) were obtained from Shanghai Aladdin biochemical technology Co., Ltd. Polyacrylonitrile (PAN) was purchased from Dow chemical group.

2.2. Electrospinning of PAN nanofibers

First, solution of PAN electrospun precursor was prepared. 2 g of PAN (MW=150000) and 15 mL of N-N dimethylformamide (DMF) was dissolved with stirring. The mixture was fully dissolved under magnetic stirring at 50 °C for 2 h to form a transparent solution. After stirring, the prepared precursor was aged overnight. The aged precursor solution was transferred into a syringe with the volume of 5 mL, then it was connected with the high-voltage electrostatic power supply and the voltage was set to 12 kV. The electrospun fibers were collected with a grounded aluminum foil. The distance between the spinneret and the receiving aluminum foil was between about 15 cm, and the flow rate of the syringe pump was 15 μL/min. The air humidity was controlled below 40% by a dehumidifier, and the fibers were collected continuously for 10 h.

2.3. Preparation of PAN-$Bi_2O_2CO_3$ nanofibers

After completing the preparation steps of PAN flexible fibers, $Bi_2O_2CO_3$ nanosheets were grown on the surface of the prepared nanofibers through alternating contact with Bi^{3+} ions and carbonate anions at room temperature. Specifically, 9.4 g of Na_2CO_3 was dissolved in 200 mL of deionized water, which was marked as solution 1. 5.5 g of $Bi(NO_3)_3 \cdot 5H_2O$ was dissolved in 200 mL of deionized water. Nitric acid was added dropwise to dissolve all the $Bi(NO_3)_3$, and it as marked as solution 2. 100 mg of PAN nanofibers were first soaked in solution 1 for 2 min, and taken out and washed in clean water. Then, it was soaked in solution 2 for 2 min, and washed again in water to remove excess ions. The above process is a growth cycle. In order to control the amount of $Bi_2O_2CO_3$ growing on the surface of the fibers, the number of cycles was adjusted.

2.4. PAN-$Bi_2O_2CO_3$-BiOI semiconductor heterojunction nanofibers

BiOI was loaded onto $Bi_2O_2CO_3$ by ion substitution. 100 mg of the above PAN-$Bi_2O_2CO_3$ nanofibers were soaked in 100 mL of deionized water dissolved with 0.1 g, 0.3 g, 0.65 g and 1.5 g KI, respectively, and the reaction time was 30 min. During this process, it can be observed that the color of the fibers gradually turns to yellow as the time becomes longer and the concentration of KI increases. After soaking, the fibers were washed twice with deionized water and anhydrous ethanol to remove the residue, and then dried in a vacuum oven at 60 °C for 2 h. The PAN-$Bi_2O_2CO_3$-BiOI obtained at four different concentrations were marked as S1 to S4, respectively. For the experimental data comparison, the experimental comparison was made by using the same method as above to prepare PAN-BiOI nanofibers with pure PAN fibers.

3. Results and discussion

3.1 Structure characterization

The crystal structures of the samples were characterized by XRD. Fig. 1 shows the XRD curve of PAN-BiOI, PAN-$Bi_2O_2CO_3$, and PAN-$Bi_2O_2CO_3$-BiOI samples with different reaction conditions. It can be observed from the XRD result that the diffraction peak of PAN-$Bi_2O_2CO_3$ corresponds to PDF#41-1488. 30.3º, 32.7º, 42.3º and 56.9º correspond to the (013), (110), (114) and (123) diffraction planes of the tetragonal $Bi_2O_2CO_3$, respectively. The diffraction peaks of $Bi_2O_2CO_3$ and BiOI can be clearly observed in the PAN-$Bi_2O_2CO_3$-BiOI heterojunction sample. The diffraction peak of BiOI (PDF#10-0445) at 29.6º, 31.6º, 39.4º, 45.3º, 55.1º correspond to (102), (110), (004), (200) and (212) crystal planes, respectively. As shown in the S1-S4 diffraction curve in the figure, it can be observed that the BiOI diffraction peak at 39.4º is gradually enhanced

with the increase of the substitution amount of BiOI, and the $Bi_2O_2CO_3$ diffraction peak at 30.3° is gradually weakened due to the formation of BiOI by Bi and I on the surface of $Bi_2O_2CO_3$, which proves the formation of $Bi_2O_2CO_3$-BiOI heterojunctions. At the same time, with the increase of the amount of BiOI on the fiber surface, the color gradually changed from white to yellow, which proved the formation of BiOI on the surface of the fibers.

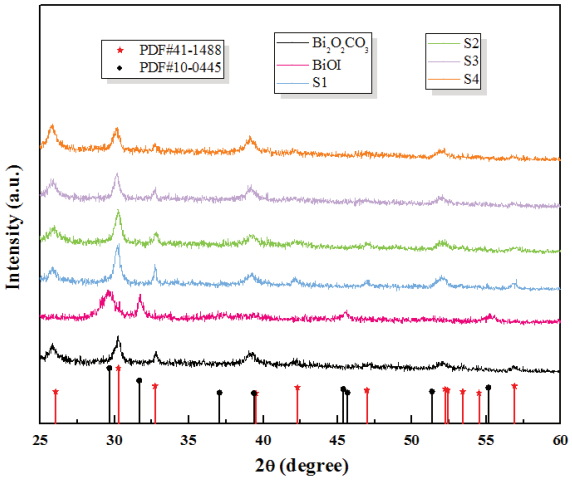

Fig. 1 X-ray powder diffraction results of PAN-BiOI, PAN-$Bi_2O_2CO_3$ and PAN-$Bi_2O_2CO_3$-BiOI samples. S1-S4 are PAN-$Bi_2O_2CO_3$-BiOI samples prepared under different KI substitution conditions, respectively

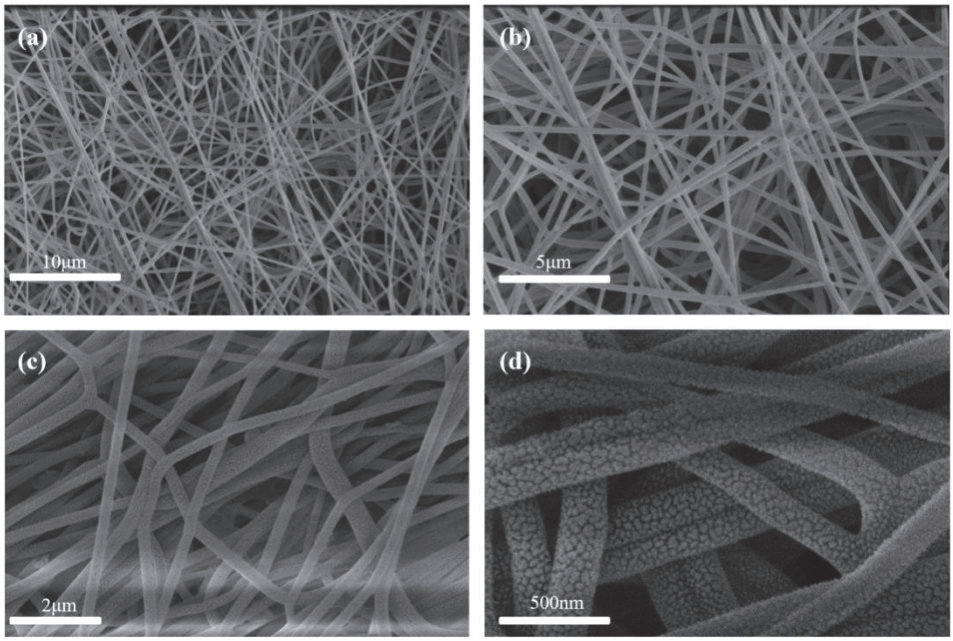

Fig. 2 SEM pictures of the PAN and PAN-$Bi_2O_2CO_3$-BiOI fibers (a) PAN, (b)-(d) PAN-$Bi_2O_2CO_3$-BiOI fibers of S3 with different magnification

3.2 Morphologies of the samples

Figure. 2 is scanning electron microscope photographs of the samples. Fig. 2(a) shows the bare

PAN fiber, which is about 200 nm in diameter and has a smooth surface. When using Na_2CO_3 and $Bi(NO_3)_3$ to alternately grow $Bi_2O_2CO_3$ on PAN surface and perform ion substitution, PAN-$Bi_2O_2CO_3$-BiOI is formed on the surface. The $Bi_2O_2CO_3$-BiOI on the outside of the PAN fiber granular and evenly covers the surface of the PAN. It can be observed from the enlarged Fig. 2(d) that the particle diameter is about 40 nm and the diameter is uniform. Fig. 3 is an X-ray energy spectrum scan of PAN-$Bi_2O_2CO_3$-BiOI fibers. It can be observed from the element overlap diagram in Fig. 3(a) that the fibers contain the main components of Bi, O, and I of $Bi_2O_2CO_3$-BiOI. From Fig. 3(a)-(d), the distribution of various elements is uniform, indicating that $Bi_2O_2CO_3$-BiOI is uniformly formed on the fiber surface.

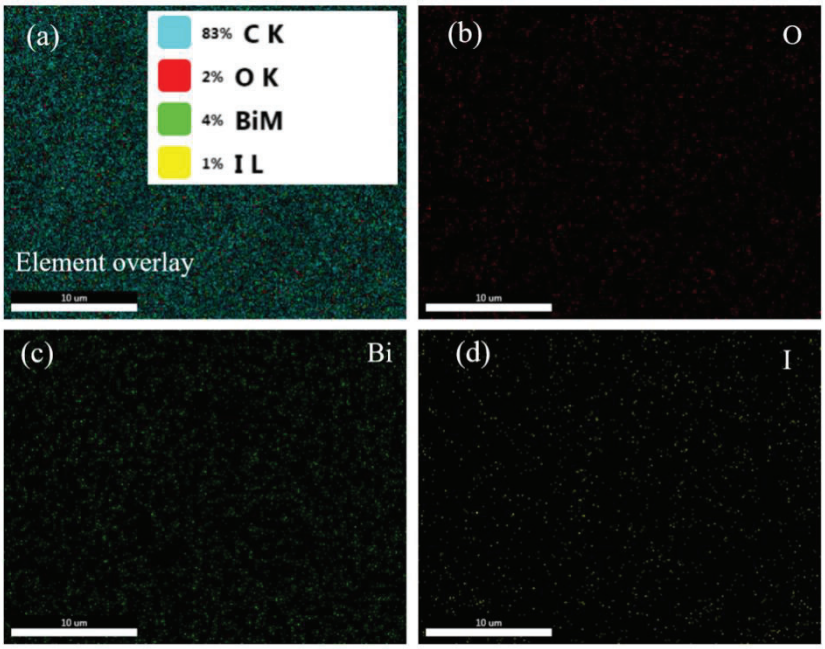

Fig. 3 X-ray energy spectrum scan of PAN-$Bi_2O_2CO_3$-BiOI nanofibers

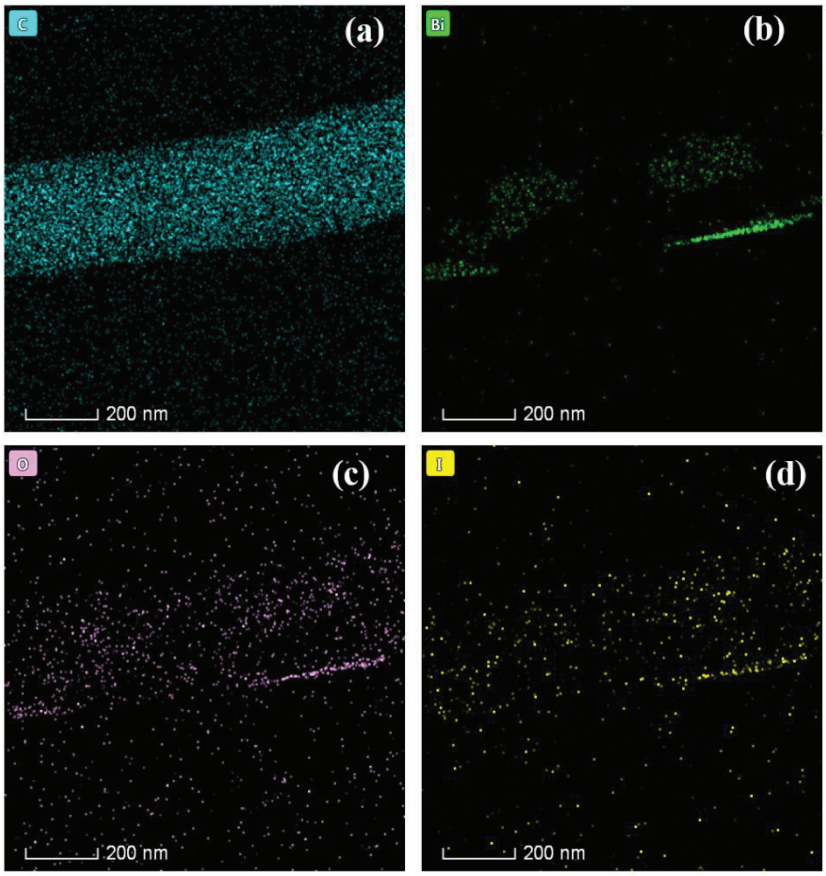

Fig. 4 TEM surface elements distribution of PAN-$Bi_2O_2CO_3$-BiOI fiber (a) C (b) Bi (c) O (d) I

To further characterize the elemental fractionation on the surface of a single fiber, the S3 sample of PAN-$Bi_2O_2CO_3$-BiOI was analyzed by transmission electron microscopy. Figure 4 is a TEM image of surface element distribution map for a single fiber, and the corresponding sample has been chopped and dispersed by ultrasonication in ethanol. Fig. 4(a) shows the distribution of carbon element. Since C element is the main element in PAN, the outline of the fiber can be seen. Fig. 4(b)-(d) are the distribution diagrams of Bi, O, and I, respectively. It can be seen that the three elements of Bi, O and I, which constitute $Bi_2O_2CO_3$-BiOI, on surface of the fiber, indicating the formation of BiOI on the surface of $Bi_2O_2CO_3$.

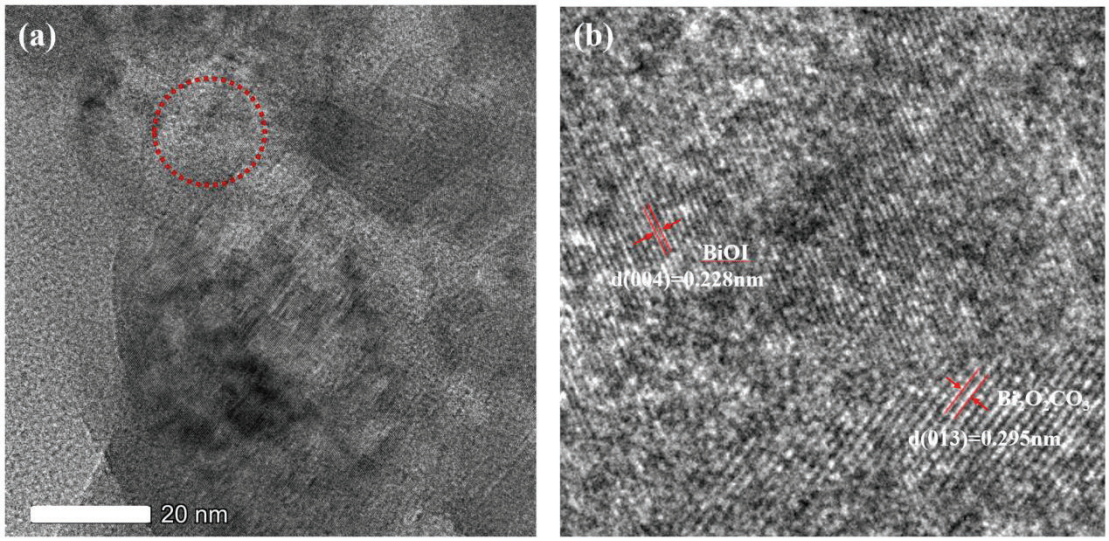

Fig. 5 HRTEM of PAN-$Bi_2O_2CO_3$-BiOI heterojunction structure (a) Image of PAN-$Bi_2O_2CO_3$-BiOI TEM (b) high resolution TEM of lattice structure of heterojunction

The $Bi_2O_2CO_3$-BiOI heterojunctions on the PAN surface was further characterized by high resolution TEM. Figure 5 is a high resolution transmission electron microscope photograph from a S3 fiber sample of PAN-$Bi_2O_2CO_3$-BiOI. Fig. 5(b) is a high-resolution analysis of the region in Fig. 5(a) where nanoparticles are retained on the surface of the PAN fiber. As shown in the figure, two different lattice fringes can be observed in Fig. 5(b). The corresponding crystal planes are (004) and (013) for BiOI and $Bi_2O_2CO_3$, respectively. And the lattice spacings of BiOI and $Bi_2O_2CO_3$ are 0.228 nm and 0.295 nm, respectively. This shows that BiOI and $Bi_2O_2CO_3$ heterojunctions are formed on the surface of PAN fibers. This is mainly due to the I^- anions taking Bi^{3+} ions in $Bi_2O_2CO_3$ to form BiOI. This surface growth reaction favors the formation of heterojunctions, which corresponds to the enhancement and weakening of the diffraction peaks of BiOI and $Bi_2O_2CO_3$ in the XRD results. In the XRD patterns, the (013) diffraction peak of $Bi_2O_2CO_3$ gradually weakened with the reaction, while the intensity of the (004) diffraction peak of BiOI overlapped with the diffraction peak of $Bi_2O_2CO_3$ was enhanced, which proved that BiOI gradually covered part of the $Bi_2O_2CO_3$ crystal plane.

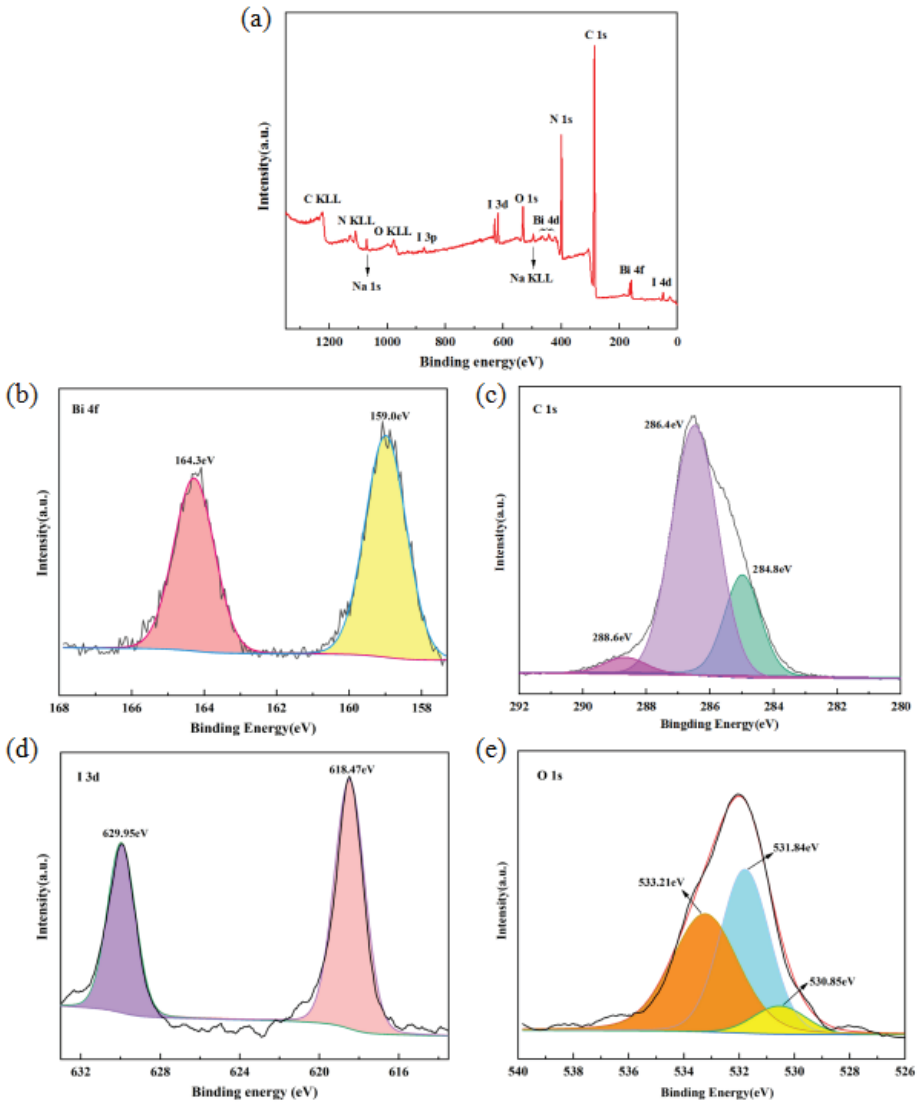

Fig. 6 X-ray photoelectron spectroscopy of PAN-$Bi_2O_2CO_3$-Bi fiber (a) Full spectrum scanning (b)-(e) Bi 4f, C 1s, I 3d, O 1s

3.3 Chemical composition and valence states of photocatalyst

To characterize the chemical composition and valence states of the nanoheterojunctions supported on the surface of PAN fibers, the fibers was characterization by X-ray photoelectron spectroscopy (XPS). The XPS spectrum of the S3 sample fiber is shown in Fig. 6. Fig. 6(a) is the full spectrum scan of the sample. It contains elements such as Bi, O, N, I, and C. This is consistent with the main components of PAN-$Bi_2O_2CO_3$-BiOI. The small peak near 435 eV corresponds to the Bi 4d orbit. The peak near 400 eV corresponds to the N 1s orbit and is related to the PAN component. Small peaks near 1220 eV, 1100eV, and 980 eV correspond to C KLL, N KLL, and OKLL, respectively. Two small peaks of 1069 eV and 495 eV correspond to Na 1s and Na KLL.

This may be caused by the adsorption of trace Na cation on the sample, but it will not significantly affect the performance of the catalyst. Fig. 6(b)-(e) are the XPS spectra of Bi 4f, C 1s, I 3d, and O 1s, respectively. In Fig. 6(b), the peaks at 164.3 eV and 159.0 eV correspond to Bi $4f_{5/2}$ and Bi $4f_{7/2}$, which should be assigned to Bi^{3+} [41]. Fig. 6(c) shows that the main peaks of C located at 288.6 eV, 286.4 eV and 284.8 eV, respectively. The peak located at 284.8 eV is usually assigned to adventitious carbon, another two weak peaks positioned at 288.6 eV and 286.4 eV corresponds to carbonate ion in $Bi_2O_2CO_3$ [24, 25]. Fig. 6(d) shows two peaks at 629.95 eV and 618.47 eV corresponds to the I anion of BiOI, which should be attributed to I $3d_{3/2}$ and I $3d_{5/2}$, respectively [42]. The XPS spectrum of O 1s in Fig. 6(e) is not singlet, which indicates that there is more than one state of O. The O 1s XPS spectrum can be fitted to three peaks at 530.85 eV, 531.84 eV and 533.21 eV. 530.85 eV corresponds to lattice oxygen anion, that is, the Bi-O bond of $[Bi_2O_2]^{2+}$ in BiOI layer. 531.84 eV corresponds to carbonic acid and 533.21 eV corresponds to the -OH bond of the surface adsorbed water [43]. These results prove the valence states of various elements in PAN-$Bi_2O_2CO_3$-BiOI from the valence aspect.

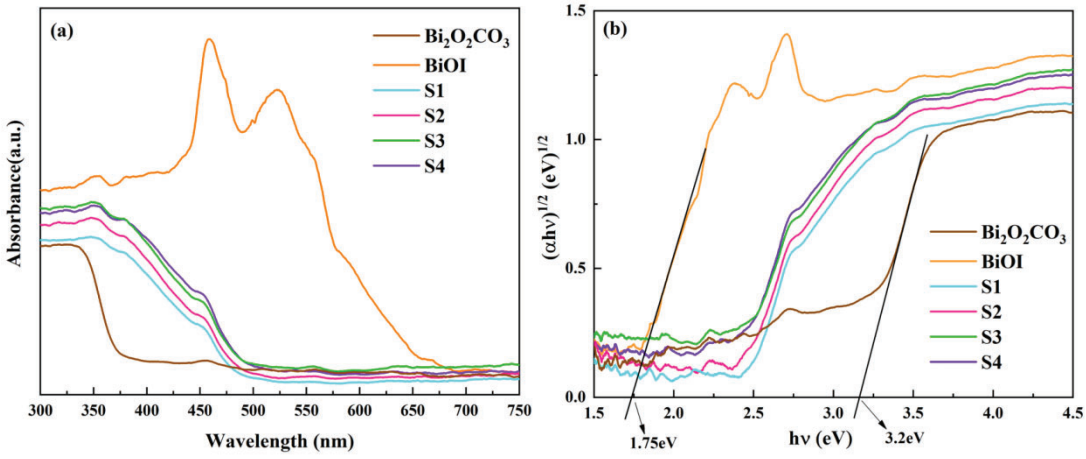

Fig. 7 (a) UV-Vis diffuse reflectance spectra of PAN-BiOI, PAN-$Bi_2O_2CO_3$ and PAN-$Bi_2O_2CO_3$-BiOI samples (b) hv-$(\alpha hv)^{1/2}$ curves of the samples

Fig. 7(a) shows the UV-vis diffuse reflectance spectra and hv-$(\alpha hv)^{1/2}$ relationship curves of PAN-BiOI, PAN-$Bi_2O_2CO_3$ and PAN-$Bi_2O_2CO_3$-BiOI photocatalyst samples. From the figure, the absorption of PAN-$Bi_2O_2CO_3$ photocatalyst is mainly in the UV region, and the band edge is around 370 nm, indicating that it has a wide band gap. The absorption of PAN-BiOI is mainly in the visible light region, and the band edge is around 650 nm, indicating that it has a narrow band gap.

When the surface of PAN-$Bi_2O_2CO_3$ undergoes ion substitution and forms $Bi_2O_2CO_3$-BiOI, it exhibits strong light absorption in the visible light range, and the absorption band edge shifts to the long wavelength, which is located between PAN-$Bi_2O_2CO_3$ and PAN-BiOI. This indicates that they constitute heterojunctions, which will facilitate the further separation of the photogenerated electron holes of BiOI. In these samples, the absorption band edge of S3 fiber loaded with $Bi_2O_2CO_3$-BiOI on PAN is around 500 nm, indicating that BiOI affects the band gap of $Bi_2O_2CO_3$ after the heterojunction is formed. The band gap of the semiconductor photocatalytic material can be calculated by the following formula [44]:

$$\alpha hv = A(hv - E_g)^{n/2}$$

where Eg, α, A, h, v are the band gap, absorption coefficient, proportionality constant, Planck constant and optical frequency, respectively. Here, n=1 for direct bandgap semiconductors, and n=4 for indirect bandgap semiconductors. Because $Bi_2O_2CO_3$ and BiOI are both indirect bandgap semiconductors, then n=4. To calculate the band gap value, PAN-$Bi_2O_2CO_3$, PAN-BiOI, and PAN-$Bi_2O_2CO_3$-BiOI should be plotted against hv-$(\alpha hv)^{1/2}$, respectively. In Fig. 7(b), the band gap value can be determined by the tangent of the curve and the intersection of the horizontal axis. It can be seen from the figure that the band gaps of PAN-BiOI and PAN-$Bi_2O_2CO_3$ are 1.75 eV and 3.20 eV, respectively. By comparison, the band gap of the PAN-$Bi_2O_2CO_3$-BiOI composite component is located at about 2.2~2.5 eV, which is between the band gap values of the two single components of BiOI and $Bi_2O_2CO_3$, indicating that heterojunctions are formed between them and the photogenerated carriers are also easier to be separated.

The valence band potential VB and conduction band potential CB of $Bi_2O_2CO_3$ and BiOI semiconductor photocatalysts were calculated using the following formulas [45]:

$$E_{VB} = X - E_e + 0.5E_g$$

$$E_{CB} = E_{VB} - E_g$$

Here, E_{VB} is the top of the valence band, X is the electronegativity, Eg is the width of forbidden band, Ee is the surface electron free energy of the hydrogen atom (4.5 eV). The X values of BiOI and $Bi_2O_2CO_3$ are 6.21 eV and 6.54 eV, respectively [46]. Since the Eg values of PAN-BiOI and PAN- $Bi_2O_2CO_3$ are 1.75 eV and 3.20 eV, respectively, after bringing the constants into the formula, the E_{VB} values of PAN-BiOI and PAN- $Bi_2O_2CO_3$ are 2.59 eV (vs. NHE) and 3.64 eV (vs. NHE), respectively. In addition, the E_{CB} values of PAN-BiOI and PAN-$Bi_2O_2CO_3$ can be obtained

as 0.84 eV (vs NHE) and 0.44 eV (vs NHE) through the conversion relationship between the conduction band and the valence band: $E_{CB}=E_{VB}-Eg$.

3.4 Catalytic performance of photocatalyst

The catalytic properties of the above photocatalysts were carried out in the visible light range. The light source used is a 300 W xenon lamp (Beijing China education Aulight technology Co., Ltd., CEL-HXF300), and a visible light filter (>420 nm) is added to the outlet of the xenon lamp. Rhodamine B (RhB) was used as the photocatalytic target at a concentration of 20 mg/L. Then, 100 mg of photocatalytic fibers were added into 50 mL of the solution. After that, photocatalysis was performed after the catalyst and RhB reached adsorption equilibrium by magnetic stirring for 30 min. 4 mL of the solution was taken out at intervals of 15 min, and the absorbance was tested after centrifugation. The absorption wavelength is 554 nm. As shown in Fig. 8(a), PAN itself does not exhibit photocatalytic properties under light irradiation. It can be seen from the results that the wide band gap $Bi_2O_2CO_3$ has certain catalytic ability under visible light. Although BiO_2CO_3 is theoretically not excited under visible light. However, there may be the following reasons for the catalytic ability of BiO_2CO_3. It is speculated that the RhB dye can absorb visible light and be excited to generate electrons. And the electrons can be adsorbed on the surface of BiO_2CO_3. Similar to dye-sensitized solar cells, excited electrons can be transferred to the surface of BiO_2CO_3 and react with absorbed O_2 and H_2O to generate $\cdot OH$ and finally it has catalytic effect [46]. The degradation rates of BiOI-supported PAN-BiOI fibers and $Bi_2O_2CO_3$-supported PAN-$Bi_2O_2CO_3$ fibers were 28% and 35% at 120 min, respectively. When BiOI was loaded on the surface of PAN-$Bi_2O_2CO_3$, the degradation rates of S1, S2, S3, and S4 were significantly improved compared with the catalysts loaded with pure components, and the catalytic efficiency of S3 was greater than 90% within 120 min. The degradation rate of S3 was 2.6 times and 3 times higher than that of PAN-$Bi_2O_2CO_3$ and PAN-BiOI, respectively.

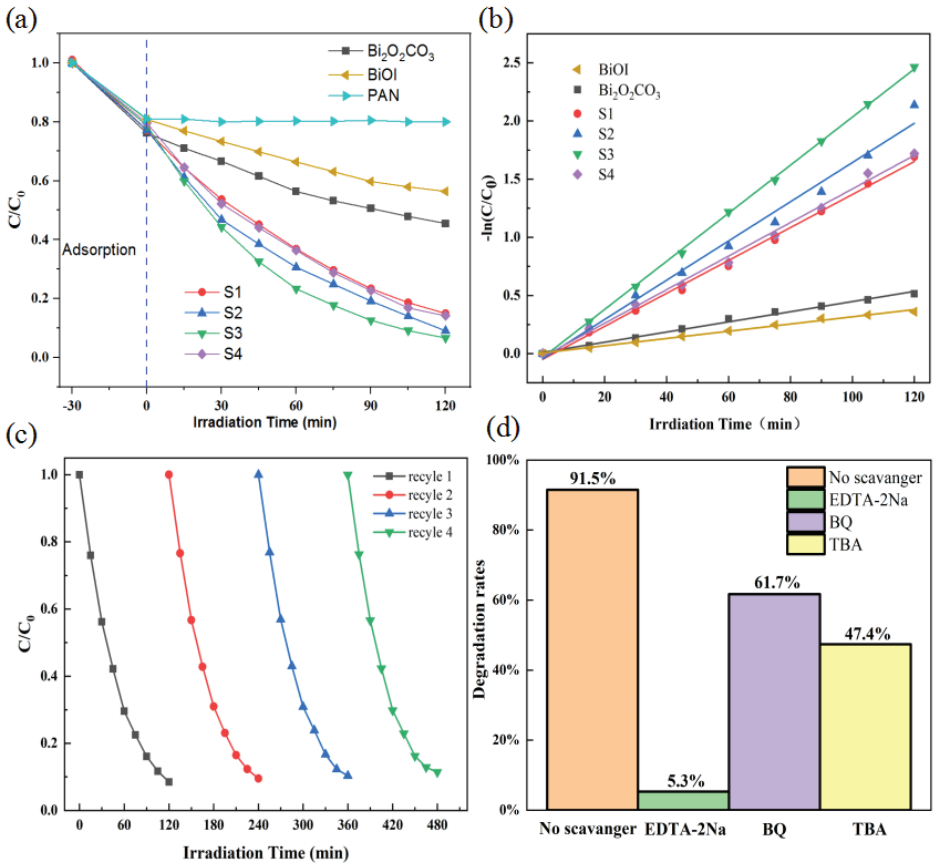

Fig. 8 Catalytic performance of photocatalyst (a) Degradation curves of RhB by different catalysts of PAN, PAN-BiOI, PAN-$Bi_2O_2CO_3$, and PAN-$Bi_2O_2CO_3$-BiOI samples of S1-S4 (b) Linear fitting diagram of first order kinetics of the above samples (c) The cyclic degradation experiment of S3

As shown in Fig. 8(b), the kinetics of the photocatalytic degradation reaction conforms to the Langmuir-Hinshelwood first-order apparent kinetic model [48]:

$$r=dC/dt=k\,k'C/(1+k'C)$$

Here, C is the residual concentration (mg L^{-1}), r is the degradation rate (mg $L^{-1}h^{-1}$), k is the reaction constant (mg $L^{-1}h^{-1}$), t is the degradation time (h), $k'$is the absorption coefficient ($L\cdot mg^{-1}$). Due to the low initial dye concentration, the above equation can be approximated to the first-order form:

$$-\ln(C/C_0)=kk't=k_{app}t$$

where C_0 is the adsorption equilibrium concentration, and k_{app} is the slope of the equation, which is the reaction constant. It can be seen from the figure that the k_{app} values of PAN-BiOI, PAN-$Bi_2O_2CO_3$, S1, S2, S3, and S4 are 0.003 min^{-1}, 0.004 min^{-1}, 0.013 min^{-1}, 0.014 min^{-1}, 0.021 min^{-1} and 0.016 min^{-1}, respectively. The photocatalytic constants of the S3 sample are 7 and 5.3 times higher than those of PAN-BiOI and PAN-$Bi_2O_2CO_3$, respectively. This shows that the

heterojunction formed by PAN-$Bi_2O_2CO_3$ and BiOI on the surface of PAN can improve the efficiency of electron-hole separation and photocatalytic speed. The reusability of the photocatalyst was tested. 4 cycles of repeated catalytic experiments were performed on the S3 sample. It can be observed from Fig. 8(c) that after several times of photocatalytic degradation of with the same concentration, the photocatalytic performance did not decrease significantly, and the final degradation rate decayed less than 4%, which indicate that the modified fiber can be reused.

3.5 Catalytic mechanism of photocatalyst

The active components produced by the PAN-$Bi_2O_2CO_3$-BiOI heterojunction in the catalytic system play an important role in photocatalysis. As shown in Fig. 9, the active species in the $Bi_2O_2CO_3$-BiOI heterostructure were investigated by trapping experiments. By adding different kinds of traps inside the catalytic system, the internally generated photoactive groups were determined. The type of the specific active group is judged by the reduction degree of photocatalytic activity. As shown in Fig. 9, after adding EDTA-2Na, benzoquinone (BQ) and tertbutanol (TBA) to the system, it was found that the degradation rate was affected by different degrees. The addition of EDTA-2Na, BQ and TBA reduced the degradation rate to 0.053, 0.617, and 0.474, respectively, within 120 min. This indicates a large amount of h^+ and some O^{2-} and ·OH are generated on the surface of the catalyst.

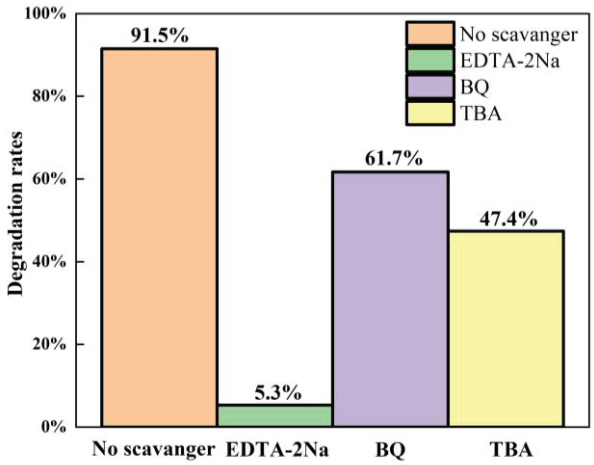

Fig. 9 The influence of reactive species on the photocatalytic degradation of RhB over sample of S3

The band structures of $Bi_2O_2CO_3$ and BiOI are shown in Fig. 10(a). Since $Bi_2O_2CO_3$ is an n-type semiconductor, its Fermi level is close to CB. BiOI is a p-type semiconductor, then its Fermi level is close to VB. When they form a p-n junction, the energy band of $Bi_2O_2CO_3$ moves downward as a whole, and the energy band of BiOI moves upward as a whole. When visible light

illuminates PAN-BiOI, electrons transition from the valence band to the conduction band, and accumulate at CB and generate holes at VB. Because its CB potential is more negative than that of $Bi_2O_2CO_3$, electrons will migrate to the CB of $Bi_2O_2CO_3$. Therefore, the existence of $Bi_2O_2CO_3$ promotes the separation of photogenerated electrons and holes of BiOI and reduces the recombination between them. Finally, electrons in the CB of $Bi_2O_2CO_3$ reduce O_2 molecules to generate·O^{2-} and ·OH, which together with the holes h^+ in the valence band of BiOI, photolysis decompose the dye.

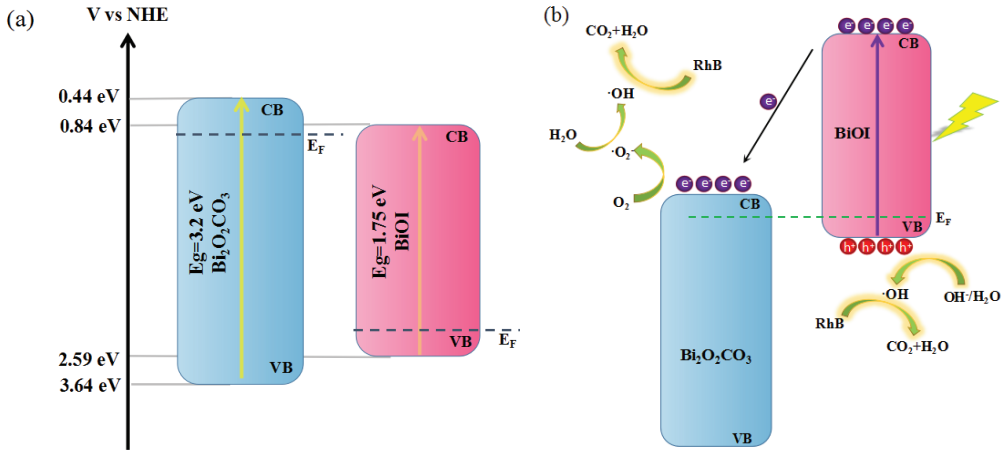

Fig. 10 (a) Energy band of $Bi_2O_2CO_3$ and BiOI (b) the formation of heterojunction and the possible charge transfer process.

4. Conclusion

In this paper, bismuth carbonate was prepared on the surface of flexible PAN fibers by alternate growth method, and bismuth iodide was formed on the surface of bismuth carbonate by ion exchange method. XRD, HRTEM and XPS results showed that the PAN fibers were successfully loaded with nano $Bi_2O_2CO_3$-BiOI heterojunctions. Visible light catalysis results demonstrate that the photocatalytic activity of flexible PAN-$Bi_2O_2CO_3$-BiOI heterojunction fibers is superior to that of single-component fibers of PAN-$Bi_2O_2CO_3$ and PAN-BiOI. The photocatalytic constants of the S3 sample are 7 and 5.3 times higher than those of PAN-BiOI and PAN-$Bi_2O_2CO_3$, respectively, and the catalytic efficiency is greater than 90% within 120 min. After 4 cycles of photocatalytic degradation with the same dye concentration, the final degradation rate decays less than 4%. Mechanism analysis showed that a large amount of h^+, O^{2-} and •OH were generated on the catalyst surface. The efficiency of separation of photogenerated electrons and holes can be significantly improved by forming the heterojunctions on the surface of PAN fibers, and the flexible

PAN-$Bi_2O_2CO_3$-BiOI fibers with high specific surface area are beneficial to be separated and recycled.

Acknowledgments

This work is supported by Fundamental Research Funds for the Central Universities (3072022CF2506); Ministry of Science and Technology "High-end Foreign Expert Introduction Program"(G2022180002); National Natural Science Foundation of China (11574061, 62065001); Natural Science Foundation of Heilongjiang Province (LH2021F019); Natural Science Foundation of Zhejiang Province of China (LGG20E040001).

References

1. J. A. Downing, S. Polasky, S. M. Olmstead, and S. C. Newbold, “Protecting local water quality has global benefits,” Nat. Commun. **12**, 2709 (2021).
2. P. Bonetti, C. Leuz, and G. Michelon, “Large−sample evidence on the impact ofunconventional oil and gas development onsurface waters,” Science **373**, 896−902 (2021).
3. M. Ashraf, I. Khan, M. Usman, A. Khan, S. S. Shah, A. Z. Khan, K. Saeed, M. Yaseen, M. F. Ehsan, M. N. Tahir, and N. Ullah, “Hematite and magnetite nanostructures for green and sustainable energy harnessing and environmental pollution control: a review,” Chem. Res. Toxicol. **33**, 1292−1311 (2020).
4. X. Yuan, Y. X. Zhang, Y. T. Zhang, P. Peng, C. L. Yuan, P. Cai, X. W. Zhang, S. W. Wang, H. B. Li, X. G. Xue, “Cyano-bridged Schottky junction of CN-TiC for enhanced photocatalytic H_2 evolution and tetracycline degradation,” Appl. Surf. Sci. **583**, 152515 (2022).
5. A. Mukherjee, A. Satish, A. Mullick, J. Rapolu, S. Moulik, A. Roy, and A. K. Ghosh, “Paradigm shift toward developing a zero liquid discharge strategy for dye−contaminated water streams: a green and sustainable approach using hydrodynamic cavitation and vacuum membrane distillation,” ACS Sustainable Chem. Eng. **9**, 6707−6719 (2021).
6. M. S. Bank, P. W. Swarzenski, C. M. Duarte, M. C. Rillig, A. A. Koelmans, M. Metian, S. Wright, J. F. Provencher, M. Sanden, A. Jordaan, M. Wagner, M. Thiel, and Y. S. Ok, “Global plastic pollution observation system to aid policy,” Environ. Sci. Technol. **55**, 7770−7775 (2021).
7. Y. Feng, X. Chen, Y. Li, H. Zhao, L. Xiang, H. Li, Q. Cai, N. Feng, C. Mo, and M. Wong, “A visual leaf zymography technique for the in situ examination of plant enzyme activity under the stress of environmental pollution,” J. Agric. Food Chem. **68**, 14015−14024 (2020).
8. Q. Huang, T. D. Canady, R. Gupta, N. Li, S. Singamaneni, and B. T. Cunningham, “Enhanced Plasmonic Photocatalysis through Synergistic Plasmonic−Photonic Hybridization,” ACS Photonics **7**, 1994−2001 (2020).
9. Y. Lin, C. Yang, S. Wu, X. Li, Y. Chen, and W. Yang, “Construction of Built−In Electric Field within Silver Phosphate Photocatalyst for Enhanced Removal of Recalcitrant Organic Pollutants,” Adv. Funct. Mater. **30**(38), 2002918 (2020).

10. J. Ma, Q. Wang, L. Li, X. Zong, H. Sun, R. Tao, and X. Fan, "Fe_2O_3 nanorods/CuO nanoparticles p−n heterojunction photoanode: Effective charge separation and enhanced photoelectrochemical properties," J. Colloid Interf. Sci. **602**, 32−42 (2021).
11. P. Zhou, J. Yu, and M. Jaroniec, "All−solid−state Z−scheme photocatalytic systems," Adv. Mater. **26**, 4920−4935 (2014).
12. H. Wang, L. Zhang, Z. Chen, J. Hu, S. Li, Z. Wang, J. Liu, and X. Wang, "Semiconductor heterojunction photocatalysts: design, construction, and photocatalytic performance," Chem. Soc. Rev. **43**, 5234−5244 (2014).
13. Q. Jiang, M. Z. Liu, C. L. Shao, X. W. Li, H. Y. Liu, X. H. Li, and Y. C. Liu, "Nitrogen doping polyvinylpyrrolidone−based carbon nanofibers via pyrolysis of g−C_3N_4 with tunable chemical states and capacitive energy storage," Electrochim. Acta **330**, 135212 (2020).
14. F. Xu, B. Zhu, B. Cheng, J. Yu, and J. Xu, "1D/2D TiO_2/MoS_2 hybrid nanostructures for enhanced photocatalytic CO_2 reduction," Adv. Opt. Mater. **23**(6), 1800911 (2018).
15. X. Yuan, S. L. Qu, X. Y. Huang, X. G. Xue, C. L. Yuan, S. W. Wang, L. Wei, and P. Cai, "Design of core−shelled g−C_3N_4@ZIF−8 photocatalyst with enhanced tetracycline adsorption for boosting photocatalytic degradation," Chem. Eng. J. **416**, 129148 (2021).
16. S. Chen, D. Huang, P. Xu, X. Gong, W. Xue, L. Lei, R. Deng, J. Li, and Z. Li, "Facet−Engineered Surface and Interface Design of Monoclinic Scheelite Bismuth Vanadate for Enhanced Photocatalytic Performance," ACS Catal. **10**(2), 1024−1059 (2020).
17. Y. Bao, W. J. Lee, J. Z. Y. Seow, H. Hara, Y. Liang, H. Feng, J. Z.C. Xu, T. T. Lim, and X. Hu, "One−Step Block Copolymer Templated Synthesis of Bismuth Oxybromide for Bisphenol A Degradation: An Extended Study from Photocatalysis to Chemical Oxidation," ACS ES T Water **1**(4), 837−846 (2021).
18. L. Yao, Z. Chen, Z. Lu and X. Wang, "Plasmonic Bi metal as a co−catalyst deposited on C−doped $Bi_6O_6(OH)_3(NO_3)_3{\cdot}1.5H_2O$ for efficient visible light photocatalysis," J. Photochem. Photobiol. A−Chem. **389**(15), 112290 (2020).
19. O. Monfort, G. Plesch, "Bismuth vanadate−based semiconductor photocatalysts: a short critical review on the efficiency and the mechanism of photodegradation of organic pollutants," Environ. Sci. Pollut. Res. **25**, 19362−19379 (2018).
20. L. Yao, H. Yang, Z. Chen, M. Qiu, B. Hu, and X. Wang, "Bismuth oxychloride−based materials for the removal of organic pollutants in wastewater," Chemosphere **273**, 128576 (2021).
21. X. Liao, X. Lan, N. Ni, P. Yang, Y. Yang, and X. Chen, "Bismuth Oxychloride Nanowires for Photocatalytic Decomposition of Organic Dyes," ACS Appl. Nano Mater. **4**(4), 3887−3892 (2021).
22. P. P Teng, Z. A. Li, S. Gao, K. Li, M. Bowkett, N. Copner, Z. Liu, and X. Yang, "Fabrication of one−dimensional Bi_2WO_6/$CuBi_2O_4$ heterojunction nanofiber and its photocatalytic degradation property," Opt. Mater. **121**, 111508 (2021).
23. S. Adhikari, S. Mandal and D. H. Kim, "1D/2D constructed Bi_2S_3/$Bi_2O_2CO_3$ direct Z-Scheme heterojunction: A versatile photocatalytic material for boosted photodegradation, photoreduction and photoelectrochemical detection of water-based contaminants," J. Hazardous Mater. **418**, 126263 (2021)

24. L. X. Li, H. J. Gao, G. R. Liu, S. F. Wang, Z. Yi, X. W. Wu, H. Yang, "Synthesis of carnation flflower-like $Bi_2O_2CO_3$ photocatalyst and its promising application for photoreduction of Cr(VI),"Adv. Powder Technol. **33,** 103481 (2022)
25. L. X. Li, X. F. Sun, T. Xian, H. J. Gao, S. F. Wang, Z. Yi, X. W. Wu, H. Yang, "Template-free synthesis of $Bi_2O_2CO_3$ hierarchical nanotubes self-assembled from ordered nanoplates for promising photocatalytic Applications," Phys. Chem. Chem. Phys. **24**, 8279−8295 (2022)
26. Z. M. Qiang, X. M. Liu, F. Li, T. H. Li, M. Zhang, H. Singh, M. Huttula and W. Cao, "Iodine doped Z-scheme $Bi_2O_2CO_3/Bi_2WO_6$ photocatalysts: facile synthesis, efficient visible light photocatalysis, and photocatalytic mechanism," Chem. Eng. J 403, 126327 (2021).
27. Z. Ni, Y. Sun, Y. Zhang, F. Dong, "Fabrication, Modification and Application of $(BiO)_2CO^{3-}$Based Photocatalysts: A Review," Appl. Surf. Sci. 365, 314−335 (2016).
28. H. Huang, X. Li, J. Wang, F. Dong, P. K. Chu, T. Zhang, and Y. Zhang, "Anionic Group Self-Doping as a Promising Strategy: Band Gap Engineering and Multi-Functional Applications of High Performance CO_3^{2-}-Doped $Bi_2O_2CO_3$," ACS Catal. 5, 4094−4103 (2015)
29. S. Bao, H. Liang, C. Li, and J. Bai, "A heterostructure BiOCl nanosheets/TiO_2 hollow−tubes composite for visible light−driven efficient photodegradation antibiotic," J. Photochem. Photobiol. A **397**, 112590 (2020).
30. D. Liu, D. Chen, N. Li, Q. Xu, H. Li, J. He, and J. Lu, "Surface Engineering of g−C_3N_4 by Stacked BiOBr Sheets Rich in Oxygen Vacancies for Boosting Photocatalytic Performance," Angew. Chem. Int. Ed. **11**(59), 4519−4524 (2020).
31. H. Wu, C. Yuan, R. Chen, J. Wang, F. Dong, J. Li, and Y. Sun, "Mechanisms of Interfacial Charge Transfer and Photocatalytic NO Oxidation on BiOBr/SnO_2 p–n Heterojunctions," ACS. Appl. Mater. Inter. **12** (39), 43741−43749 (2020).
32. S. Rieger, T. Fürmann, J. K. Stolarczyk, and J. Feldmann, "Optically Induced Coherent Phonons in Bismuth Oxyiodide (BiOI) Nanoplatelets," Nano Lett. **21** 7887−7893 (2021).
33. H. Zhu, C. Wang, X. Xiao, Z. Chen, Y. Wang, S. Xiao, Y. Li, and J. He, "Ultrafast saturable absorption of BiOI nanosheets prepared by chemical vapor transport," Opt. Lett. **46**(23), 6006−6009 (2021).
34. M. O. Olagunju, E. M. Zahran, J. M. Reed, E. Zeynaloo, D. Shukla, J. L. Cohn, B. Surnar, S. Dhar, L. G. Bachas, and M. R. Knecht, "Halide Effects in $BiVO_4$/BiOX Heterostructures Decorated with Pd Nanoparticles for Photocatalytic Degradation of Rhodamine B as a Model Organic Pollutant," ACS Appl. Nano Mater. **4**(3), 3262−3272 (2021).
35. M. Arumugam, M. Y. Choi, "Recent progress on bismuth oxyiodide (BiOI) photocatalyst for environmental remediation," J. Ind. Eng. Chem. **81**, 237−268 (2020).
36. Y. Peng, H. Z. Qian, N. N. Zhao and Y. Li, "Synthesis of a Novel 1D/2D $Bi_2O_2CO_3$–BiOI eterostructure and Its Enhanced Photocatalytic Activity," Catalysts **11**, 1284 (2021)
37. P. Y. Song, M. Xu, W. D. Zhang, "Sodium citrate-assisted anion exchange strategy for construction of $Bi_2O_2CO_3$/BiOI photocatalysts," Mater. Res. Bull. **62**, 88-95 (2015)
38. S. Ponce−Alcántara, D. Martín−Sánchez, A. Pérez−Márquez, J. Maudes, N. Murillo, and J. García−Rupérez, "Optical sensors based on polymeric nanofibers layers created by electrospinning," Opt. Mater. Express **8**(10), 3163−3175 (2018).

39. V. O. Odhiambo, C. R. M. Mustafa, L. B. Thong, Z. Kónya, and I. M. Szilágyi, “Preparation of TiO_2/WO_3/C/N composite nanofibers by electrospinning using precursors soluble in water and their photocatalytic activity in visible light,” Nanomaterials **11**, 351 (2021).
40. H. Y. Liu, C. H. Han, C. L. Shao, S. Yang, X. W. Li, B. Li, X. H. Li, J. G. Ma, and Y. C. Liu, “$ZnO/ZnFe_2O_4$ Janus Hollow Nanofibers with Magnetic Separability for Photocatalytic Degradation of Water−Soluble Organic Dyes,” ACS Appl. Nano Mater. **2**(8), 4879−4890 (2019).
41. S. Ni, T. Zhou, H. Zhang, Y. Cao, P. Yang, “$BiOI/BiVO_4$ Two-Dimensional Heteronanostructures for Visible-Light Photocatalytic Degradation of Rhodamine B,” ACS Appl. Nano Mater **1**, 5128−5141 (2018).
42. Z. Liu, W. Xu, J. Fang, X. Xu, S. Wu, X. Zhu, and Z. Chen, “Decoration of BiOI quantum size nanoparticles with reduced graphene oxide in enhanced visible−light−driven photocatalytic studies,” Appl. Surf. Sci. **259**(15), 441−447 (2012).
43. A. Phuruangrat, P. Dumrongrojthanath, S. Thongtem, and T. Thongtem, “Hydrothermal synthesis of I−doped Bi_2WO_6 for using as a visible−light−driven photocatalyst,” Mater. Lett. **224**, 67−70 (2018).
44. J. Choi, D. A. Reddy, and T. K. Kimn, “Enhanced photocatalytic activity and anti−photocorrosion of AgI nanostructures by coupling with graphene−analogue boron nitride nanosheets,” Ceram. Int. **41**(10), 13793−13803 (2015).
45. D.A. Reddy, S. Lee, J. Choi, S. Park, R. Ma, H. Yang, and T. K. Kim, “Green synthesis of AgI−reduced graphene oxide nanocomposites: toward enhanced visible−light photocatalytic activity for organic dye removal,” Appl. Surf. Sci. **341**, 175−184 (2015).
46. L. Chen, S. F. Yin, S. L. Luo, R. Huang, Q. Zhang, T. Hong, and Peter C. T. Au, “$Bi_2O_2CO_3$/BiOI Photocatalysts with Heterojunctions Highly Efficient for Visible-Light Treatment of Dye-Containing Wastewater,” Ind. Eng. Chem. Res. , **51**, 6760−6768 (2012)
47. H. Yang, “A short review on heterojunction photocatalysts: Carrier transfer behavior and photocatalytic mechanisms,” Mater. Res. Bull. **142**, 111406 (2021).
48. X. Zhang, C.L. Shao, X. Li, N. Lu, K. Wang, F. Miao, and Y. Liu, “In_2S_3/carbon nanofibers/Au ternary synergetic system: hierarchical assembly and enhanced visible−light photocatalytic activity,” J. Hazard. Mater. **283**, 599−607 (2015).